Translational Oncology
www.transonc.com
Volume 3 Number 4 August 2010 pp. 252–263

Monitoring the Effect of Docetaxel Treatment in MCF7 Xenografts Using Multimodal *In Vivo* and *Ex Vivo* Magnetic Resonance Methods, Histopathology, and Gene Expression[1]

Else Marie Huuse*, Line Rørstad Jensen*,
Pål Erik Goa*,†, Steinar Lundgren*,‡,
Endre Anderssen§, Anna Bofin¶,
Ingrid Susann Gribbestad* and Tone Frost Bathen*

*Department of Circulation and Medical Imaging, Norwegian University of Science and Technology, Trondheim, Norway; †Department of Radiology, St. Olav's University Hospital, Trondheim, Norway; ‡Department of Oncology, St. Olav's University Hospital, Trondheim, Norway; §Department of Cancer Research and Molecular Medicine, Norwegian University of Science and Technology, Trondheim, Norway; ¶Department of Laboratory Medicine, Children's and Women's Health, Norwegian University of Science and Technology, Trondheim, Norway

Abstract

The purpose of this study was to evaluate the sensitivity of dynamic contrast-enhanced magnetic resonance imaging (DCE-MRI), diffusion-weighted (DW)-MRI, *in vivo* MR spectroscopy (MRS), and *ex vivo* high-resolution magic angle spinning (HR MAS) MRS for the detection of early treatment effects after docetaxel administration. Docetaxel is an antitumor agent that leads to mitotic arrest, apoptosis, and mitotic catastrophe cell death. Gene expression analysis was performed to detect altered regulation in gene expression pathways related to docetaxel treatment effects. Histopathology was used as a measure of alterations in apoptosis and proliferation due to docetaxel. Experiments were performed using MCF7 mouse xenografts, randomized into a docetaxel (30 mg/kg) treatment group and a control group given saline. MRI/MRS was performed 1 day before treatment and 1, 3, and 6 days after treatment. Parametric images of the extracellular extravascular volume fraction (v_e) transfer constant (K^{trans}) and the apparent diffusion coefficient (ADC) were calculated from the DCE-MRI and DW-MRI data. Biopsies were analyzed by HR MAS MRS, and histopathology and gene expression profiles were determined (Illumina). A significant increase in the ADC 3 and 6 days after treatment and a significant decrease in total choline and a higher v_e were found in treated tumors 6 days after treatment. No significant difference was found in the K^{trans} between the two groups. Our results show that docetaxel induces apoptosis and decreases proliferation in MCF7 xenografts. Further, these phenomena can be monitored by *in vivo* MRS, DW-MRI, and gene expression.

Translational Oncology (2010) 3, 252–263

Introduction

More than 1 million women worldwide are diagnosed with breast cancer annually [1]. Recent advances in cancer therapy have aimed to optimize treatment strategies individually. Docetaxel is used clinically for neoadjuvant treatment of advanced breast carcinomas [2] to decrease tumor size before surgery and improve the effectiveness of systemic treatment by fighting micro metastatic disease at an early stage [2,3]. Clinical assessment of tumor sensitivity to neoadjuvant chemotherapy is performed within 3 to 4 months (i.e., after three to four cycles given each 3 weeks) by assessing changes in tumor volume [4]. New methods having the possibility to predict tumor response

Address all correspondence to: Else Marie Huuse, MSc, Department of Circulation and Medical Imaging, Norwegian University of Science and Technology, 7489 Trondheim, Norway. E-mail: else.m.huuse@ntnu.no

[1] The work presented is sponsored by the Research Council of Norway, grant nos. 186479, 183379, and 175459. The complementary DNA microarray work was done with support from the National Microarray Technology Platform (Norwegian Microarray Consortium), which is supported by the Functional Genomic Program (FuGE), Research Council of Norway.

Received 7 December 2009; Revised 17 March 2010; Accepted 22 March 2010

DOI 10.1593/tlo.09322

earlier render earlier optimized treatment strategies. This would reduce health costs and unnecessary adverse effects and increase patient survival.

Docetaxel is a microtubule-stabilizing agent that induces polymerization of tubulin monomers [5], leading to mitotic arrest in the cell cycle. Choline (Cho) metabolites have been investigated as biomarkers for cell proliferation and tumor metabolism [6–9]. *In vivo* magnetic resonance spectroscopy (MRS) provides quantitative metabolite information and is thus a promising tool for monitoring changes induced by treatment. By using high-resolution magic angle spinning (HR MAS) MRS on intact tissue samples, more detailed metabolite profiles can be obtained. Various studies have revealed an increased Cho uptake, an upregulated activity of choline kinase and an increased level of phosphocholine (PCho) in cancer cells [10–12]. A previous study in our laboratory observed decreased choline metabolite levels in docetaxel-treated tumors using *in vivo* MRS and *ex vivo* HR MAS MRS [6].

After mitotic arrest induced by treatment, tumor cells generally enter apoptosis or undergo mitotic catastrophe cell death [13,14]. The motion of water molecules is restricted by cell membranes and macromolecules. Because of this, changes in diffusion-weighted (DW) MRI may be an effective early biomarker for monitoring docetaxel treatment effects. Successful anticancer therapies have been observed to cause early increases in the tumor apparent diffusion coefficient (ADC) in both animals and humans [15–18]. DW-MRI may monitor docetaxel effects in subtumor areas and differentiate necrotic and viable tissue [19].

In addition to induced cell death, docetaxel inhibits several endothelial cell functions, impairing the development of essential tumor vasculature [20]. Dynamic contrast-enhanced magnetic resonance imaging (DCE-MRI) is a widely used tool for evaluating tumor vasculature. Contrast enhancement in tumor tissue depends on factors such as tumor vasculature, tissue perfusion, vessel permeability, and the volume of the extracellular extravascular space. The contrast enhancement curves can be analyzed either empirically [21] or with model-based quantitative methods [6,22]. Several studies have shown decreased contrast enhancement [21,23,24] and a decreased K^{trans} [18,25] after successful treatment. Jensen et al. [6] showed a slight decrease in K^{trans} in MCF7 xenografts due to docetaxel treatment.

When a tumor responds to therapy, a cascade of different incidents is actuated. The cytostatic effect of docetaxel will affect the tumor microenvironment, which, in turn, might affect the tumor gene expression profile. Gene expression analysis gives information about processes controlled at the messenger RNA level and might therefore add valuable information for understanding treatment effects detected by MRS, DCE-MRI, and DW-MRI.

Because early treatment monitoring may provide important information about patient management, the purpose of this study was to evaluate DCE-MRI, DW-MRI, *in vivo* MRS, and *ex vivo* HR MAS MRS as tools for detecting early effects of docetaxel treatment. Gene expression analysis using Illumina microarray (Illumina, Inc, San Diego, CA) was performed to study the underlying molecular mechanisms. Proliferation and apoptotic index, determined by histopathology, were used as measures for docetaxel treatment effects.

Materials and Methods

Mice and Tumors

Human MCF-7 (ATCC-HTB-22; American Type Culture Collection, Manassas, VA) breast cancer cells were cultured as recommended by the supplier. Female 6-week-old athymic mice (BalbC/c *nu/nu*; Møllergård, Denmark; mean weight, 20 g) were allowed to acclimatize for 1 week and cared for as previously described [6]. A 17β-estradiol pellet (0.72 mg, 90 days release; Innovative Research of America, Sarasota, FL) was implanted subcutaneously into the neck to facilitate optimal tumor growth for the estrogen receptor–positive MCF7 cells. Three weeks later, xenografts were initiated by subcutaneously injecting MCF7 cells (5×10^6 suspended in 0.5 ml of BD Matrigel Matrix; BD Biosciences, Bedford, MA) into the flank of the right hind leg.

Two perpendicular tumor diameters (*a* and *b*) were measured three times a week to follow tumor progression. Tumor volumes were calculated as vol = $\pi ab^2/6$, the volume of a prolate ellipsoid, assuming the third diameter to be equal to the shorter of the two measured. Seven weeks after implantation, 18 mice with a volume of 207 ± 89 mm^3 (mean ± SD) were included in the study and randomized into two groups (treatment group $n = 12$, controls $n = 6$). Seven mice (treatment group $n = 4$, controls $n = 3$) were examined by MRI 1 day before treatment (Figure 1). The day after MRI, mice in the treatment group were given intraperitoneal (i.p.) injections of 30 mg/kg docetaxel (Taxotere; Aventis Pharmaceuticals, Degenham, UK; $n = 12$), whereas controls were given 15 ml/kg saline ($n = 6$) i.p. The dose was selected

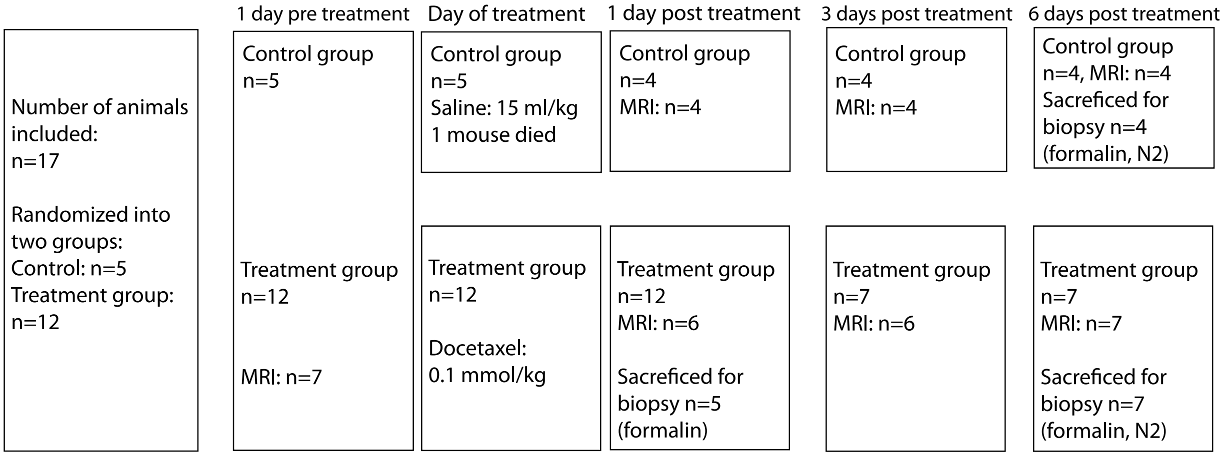

Figure 1. Seven mice were examined by MRI/MRS 1 day before treatment, 12 mice were treated with intraperitoneal (i.p.) injection of docetaxel, and 6 mice were given saline. Posttreatment MRI/MRS examinations were performed 1, 3, and 6 days after treatment.

based on a previous study [6]. The schedule for imaging and biopsy harvest is illustrated in Figure 1. Mice were killed by cervical dislocation, and biopsies were fixed in formalin (4%, 7 months). At day 6 after treatment, two additional samples from each tumor were stored in liquid nitrogen and later used for HR MAS MRS and microarray analysis, respectively.

Estrogen pellet implantation and xenograft initiation were performed under anesthesia (Haldol-Midazolam-fentanyl-sterile water, 2:3:3:4, 0.15 ml/20-g body weight). During the *in vivo* MR experiments, the mice were anesthetized with Hypnorm-Dormicum-sterile water (1:1:2, 0.16 ml/20-g body weight). Respiration rate and temperature were monitored during MRI/MRS. The animal protocol was approved by The National Animal Research Authority.

In Vivo *MRI and MRS Examination*

The *in vivo* MR examinations were performed on a 7.05-T horizontal bore magnet (BioSpec; Bruker, Ettlingen, Germany) with a quadrature surface coil. The MRI protocol included measurement of precontrast T_1 values (T_{10}) using a series of spin-echo images with varying repetition times (RARE [Bruker]: echo time (TE) = 12.5 milliseconds; repetition time (TR) = 150, 600, 1200, 2500, 7500 milliseconds; RARE factor of 2; 20 × 20 mm^2 field of view [FOV]; 128 × 128 matrix; slice thickness of 0.7 mm) followed by a DCE-MRI series of 200 T1-weighted images with identical geometry and a temporal resolution of 4.8 seconds (RARE [Bruker]: TE = 7 milliseconds, TR = 200 milliseconds, and RARE factor of 4). All tumors were imaged with four axial slices to cover the largest tumor area. A bolus dose of 0.1 mmol/kg gadodiamide (Gd-DTPA-BMA, diluted 1:10 in saline; Omniscan, GE Healthcare, Norway) was injected intravenously during 4 seconds at the start of the 10th repetition. After the dynamic series, anatomic postcontrast images were acquired (FLASH [Bruker]: TE = 5.4 milliseconds, TR = 350 milliseconds, 20 × 20 mm^2 FOV, 128 × 128 matrix, slice thickness of 0.7 mm, and 12 slices). Before further analysis, the signal-to-noise ratio was improved by averaging 2 × 2 voxels in the dynamic series. Regions of interest (ROIs) enveloping the tumor were defined with reference to the high-resolution postcontrast images. The signal enhancement curve for each averaged voxel inside the ROI was analyzed to determine the relative signal intensity 1 minute after injection ($\text{RSI}_{1\ \text{min}}$), the area under the curve during the first 2 minutes ($\text{AUC}_{0\text{-}2\ \text{min}}$), and time to peak. To ensure that the conditions for a two-compartment model were fulfilled, voxels with an $\text{RSI}_{1\ \text{min}}$ less than 80% 1 minute after injection were excluded from further analysis [26]. The signal intensity was converted to contrast agent concentration as previously described [6]. Assuming a two-compartment model and a population-based biexponential vascular input function [27], v_e and K^{trans} were estimated based on the model of Tofts [22]. Voxels with K^{trans} <0 and >1 and v_e >1 were excluded because of poor curve fitting. Median K^{trans}, v_e, and the mean value of the upper 10% RSI were estimated [28]. The MR images were analyzed using in-house software developed in MATLAB (The MathWorks, Inc, Natick, MA).

DW-MRI data were obtained using diffusion-sensitizing gradients and echo planar imaging with fat suppression and five different *b* values (0, 100, 300, 600, and 1000 sec/mm^2) with three orthogonal gradient directions (*x*, *y*, *z*) (TE = 32 milliseconds, TR = 3000 milliseconds, diffusion separation time = 14 milliseconds, diffusion gradient duration = 7 milliseconds, 20 × 20 mm^2 FOV, 128 × 128 matrix, slice thickness of 2 mm, 2 slices). To improve image quality, an EPI adjust macro (Bruker PV.4.0) was used to optimize the acquisition delay correction. ADC maps were calculated based on signal intensity as a monoexponential function of the *b* values (Bruker PV.4.0). ROIs enveloping the tumor were obtained with support from the high-resolution postcontrast images, and the median ADC values were determined for each ROI.

In vivo MRS volumes of 3 × 3 × 3 mm^3 were located within the tumors. A cube with sides 3 to 5 mm enveloping the MRS volume was automatically shimmed. Spectra were recorded by a point resolved spectroscopy sequence (TE = 20 milliseconds and TR = 3000 milliseconds) with outer volume and water suppression. The free induction decay was acquired in 4000 points during 511 milliseconds (128 averages). A 4-Hz exponential line broadening was performed before zeropadding and Fourier transformation into 8000 points. The spectra were phase-corrected, and chemical shifts were referenced to the total choline (tCho) peak (3.2 ppm). Baseline offset was corrected by subtracting the mean of the noise (8-9 ppm). Normalization was performed by dividing by the standard deviation of the noise (8-9 ppm). The relative concentration of tCho was achieved by integrating between the two nearest local minima of the peak at 3.2 ppm.

Ex Vivo *HR MAS MRS*

HR MAS MR spectra were obtained using a BrukerAvance DRX600 spectrometer with the gradient aligned with the magic angle axis (Bruker BioSpin). Tumor biopsies (mean weight ± SD of 14.6 ± 2.3 mg) were cut on ice to fit the MAS rotor (50 μl, 4-mm diameter), and 40 μl of buffer (D_2O containing 1.37 mM trimethylsilyl-3-propionic acid sodium salt d_4, formate 10.98 mM) was added. The rotors were weighed before and after assembly.

Single-pulse–acquired and spin-echo spectra were acquired as previously described [29]. All spectra were recorded within 55 minutes (mean ± SD of 41 ± 10 minutes, spin rate of 5 kHz, at 4°C). Spectra were processed with an exponential filter of 0.3 Hz, and the phase and baseline offset were corrected. Trimethylsilyl-3-propionic acid sodium salt d_4 served as a chemical shift reference. The peak areas of glycerophosphocholine (GPC), PCho, Cho, and formate were calculated by peak fitting the pulse-acquired spectra (PeakFit; SeaSolve Software, Inc, San Jose, CA). The formate peak (corrected for biopsy weight and added buffer) served as a reference for quantification and multivariate data analysis.

Histopathologic Examinations

The formalin-fixed and paraffin-embedded biopsies were cut into 4-μm sections and stained with hematoxylin, eosin, and saffron (HES). Immunohistochemical staining for the proliferation marker Ki-67 was carried out using MIB1 (monoclonal mouse anti-rat Ki-67 antigen; DakoCytomation, Glostrup, Denmark) and for apoptotic cells using M30 Cytodeath (Roche Diagnostics GmbH, Penzberg, Germany) according to the manufacturers' instructions after antigen retrieval by pressure cooking. The HES-, MIB1-, and M30-stained sections were examined microscopically by an experienced pathologist. The number of mitotic cells was counted in the HES-stained sections (per 10 FOVs at 400× magnification), and the proliferation index and apoptotic index were estimated as the number of MIB1- and M30-positive nuclei, respectively, per 1000 tumor cells.

RNA Isolation and Gene Expression

Total RNA was extracted from control (*n* = 5) and treated (*n* = 6) tumors harvested 6 days after treatment (mean weight ± SD of 53 ± 23 μg) using the Magna Pure LC RNA isolation kit II for tissue

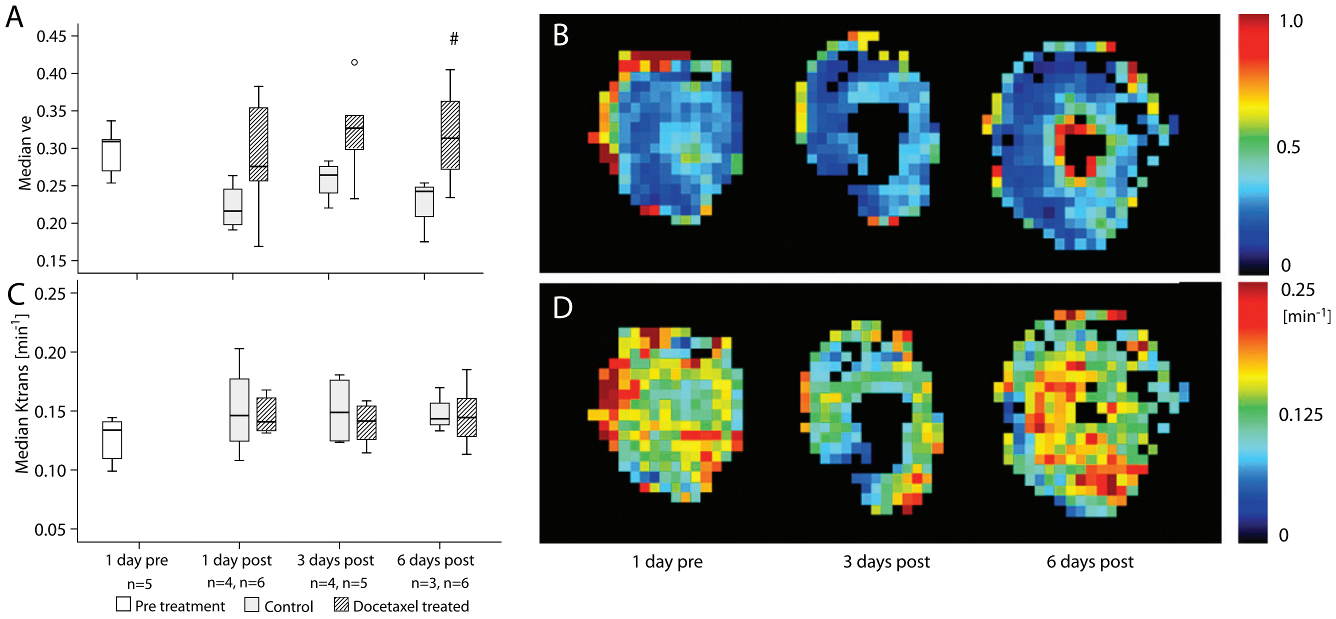

Figure 2. (A and C) Box plots of median v_e and K^{trans} values for control and treated tumors 1 day before (pre) treatment and 1, 3, and 6 days after (post) treatment. (B and D) v_e and K^{trans} maps from about the same region in a treated tumor 1 day before treatment and 3 and 6 days after treatment. ○ indicates observations of 1.5 interquartile ranges from the end of the box; $^{\#}$, significant difference (*t* test) between treated and control on the same day.

(Roche). Cells were lysed with 600 ml of lysing buffer, and RNA was isolated with 350 μl of lysate supernatant in accordance with the manufacturer's protocol. Total RNA amount and quality was examined with a Nanodrop ND-1000 spectrophotometer (Nanodrop Technologies, Wilmington, DE) and an Agilent 2100 Bioanalyzer RNA 6000 pico kit (Agilent Technologies, Santa Clara, CA).

Total RNA (300-500 ng) was converted to complementary DNA using the Illumina TotalPrep RNA Amplification Kit. Complementary DNA (750 ng) was hybridized to a human Ref-8 BeadChip Array (Illumina, Inc) following the Illumina Whole-Genome Gene Expression Protocol for BeadStation; gene expression analysis was performed using the Sentrix BeadChip and BeadStation system from Illumina. Data were $\log_2$-transformed and quantile-normalized using R (version 2.6.1; The R Foundation for Statistical Computing http://www.gnu.org/licenses/gpl.html). Significantly differentially expressed genes were identified using a modified *t* test [30], correcting for multiple testing using the method of Benjamini and Hochberg [31] to arrive at false discovery rate *P* values.

The gene data set was exported for gene set enrichment analysis (GSEA, Broad Institute of MIT and Harvard, MA) [32]. The Kyoto

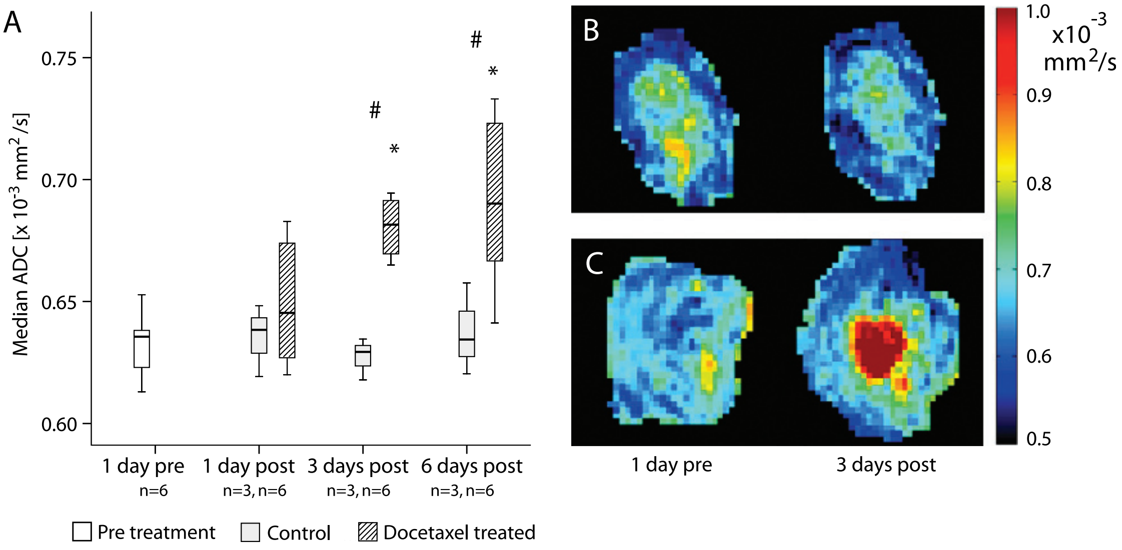

Figure 3. (A) Box plot showing progress in the median ADC 1 day before (pre) treatment and 1, 3, and 6 days after (post) treatment. Asterisk (*) indicates significant difference (Dunnet) between before and after treatment; $^{\#}$, significant difference (*t* test) between treated and control on the same day. (B and C) ADC maps from a control tumor and a treated tumor 1 day before (pre) treatment and 3 days after (post) treatment.

Encyclopedia of Genes and Genomes [33–35] was used to define the *a priori* gene sets. In addition, a gene set was manually created by including genes involved in PCho metabolism described by Eliyahu et al. [36]: choline high-affinity transporter 1 (*SLC5A7*), organic cation transporter 1 (*SLC22A1*), organic transporter 2 (*SLC22A2*), choline transport-like protein 1 (*CTL1*), phospholipase D (*PLD*), choline kinase α (*CHKA*), and choline kinase β (*CHKB*). For the GSEA, $P <$ .05 and false discovery rate <.25 were considered significant.

Statistical and Multivariate Analysis

Statistical analyses were performed using SPSS 15.0 (SPSS, Inc, Chicago, IL). Independent-sample *t* test was used to compare the control group to the treatment group on each day after treatment, and one-way analysis of variance test (Dunnet) was used to compare posttreatment and pretreatment parameters in each group. Unequal variances were assumed. Outliers were identified using the extreme studentized deviate procedure with 95% confidence interval, assuming normal distribution verified visually by a Q-Q plot.

Pearson correlation coefficients between the histopathologic parameters (number of mitoses, proliferation index, and apoptotic index) and the *in vivo* MR parameters (median K^{trans}, median v_e, median ADC, and tCho) were calculated.

The relationship between HR MAS MR spectra (spectral region 0.5-4.7 ppm) and histopathologic parameters was investigated by partial least squares (PLS) regression using The Unscrambler (CAMO Software AS, Oslo, Norway). In PLS, principal components (PCs) are derived to maximize the covariance between the spectra (X) and class-assigned target values (Y). For proliferation index and number of mitoses as target values, the spin-echo spectra were used as input, whereas pulse-acquired spectra were used for the apoptotic index. PLS was carried out using full cross-validation and mean centering, and the number of PCs retained was determined by the PC, minimizing the error of prediction. Score plots and loading profiles were examined.

Results

In Vivo MRI and MRS Examinations

There were no significant changes in tumor growth based on outer tumor volume measurements during the 6-day posttreatment period.

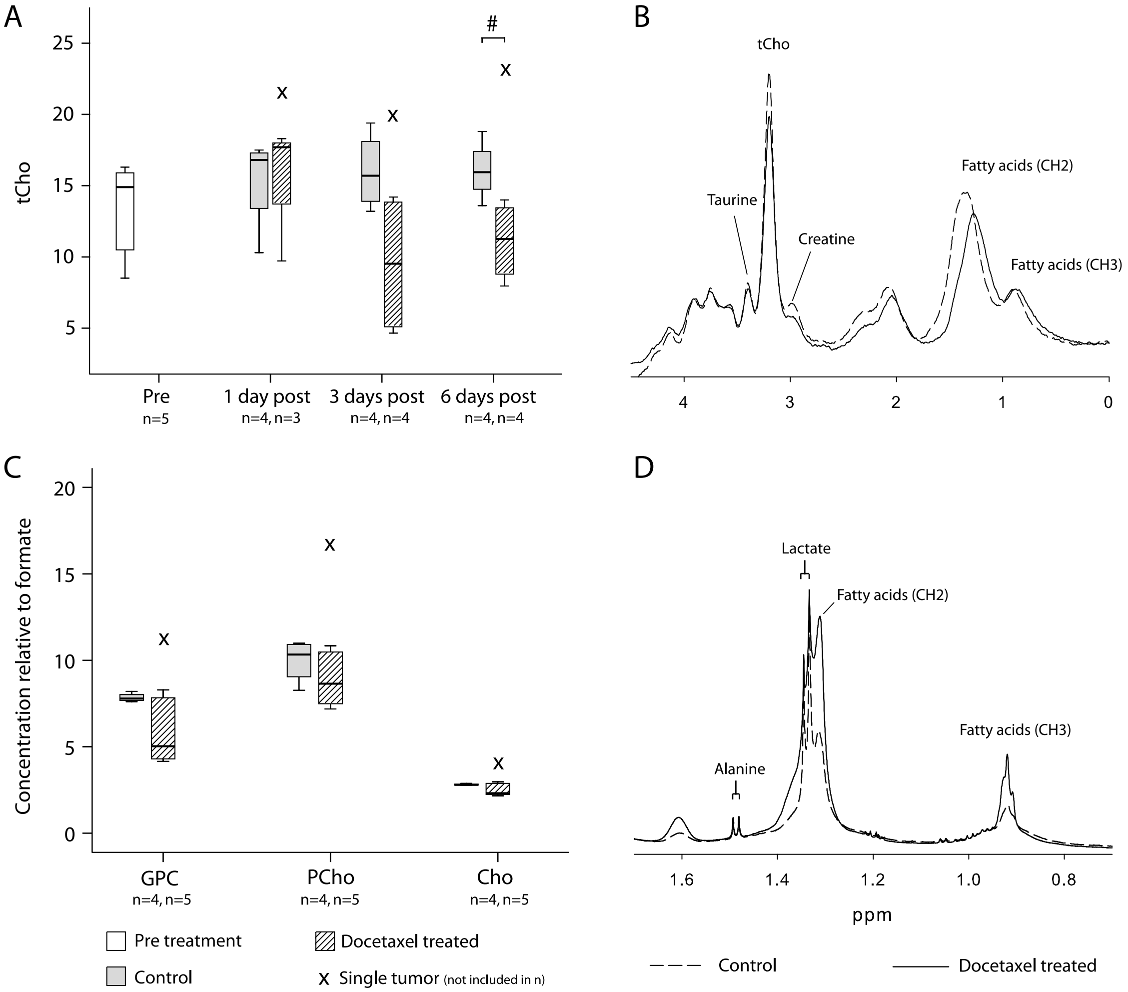

Figure 4. (A) *In vivo* tCho levels showing a significant difference between treated and control tumors 6 days after treatment. (B) Mean *in vivo* MR spectra from the two groups showing a shift in parts per million (ppm) values for the fatty acids and a decrease in tCho after docetaxel treatment. (C) Metabolite concentrations estimated from *ex vivo* HR MAS MR spectra relative to formate. There was a trend for the concentration of all choline-containing metabolites to decrease. (D) Mean HR MAS MR spectra of treated and control tumors 6 days after treatment. The treated tumors have a higher content of $-(CH_2)_n$ and $-CH_3$ fatty acids. X indicates a single tumor excluded from the statistical analysis; $^{\#}$, significant difference (*t* test) between the two groups.

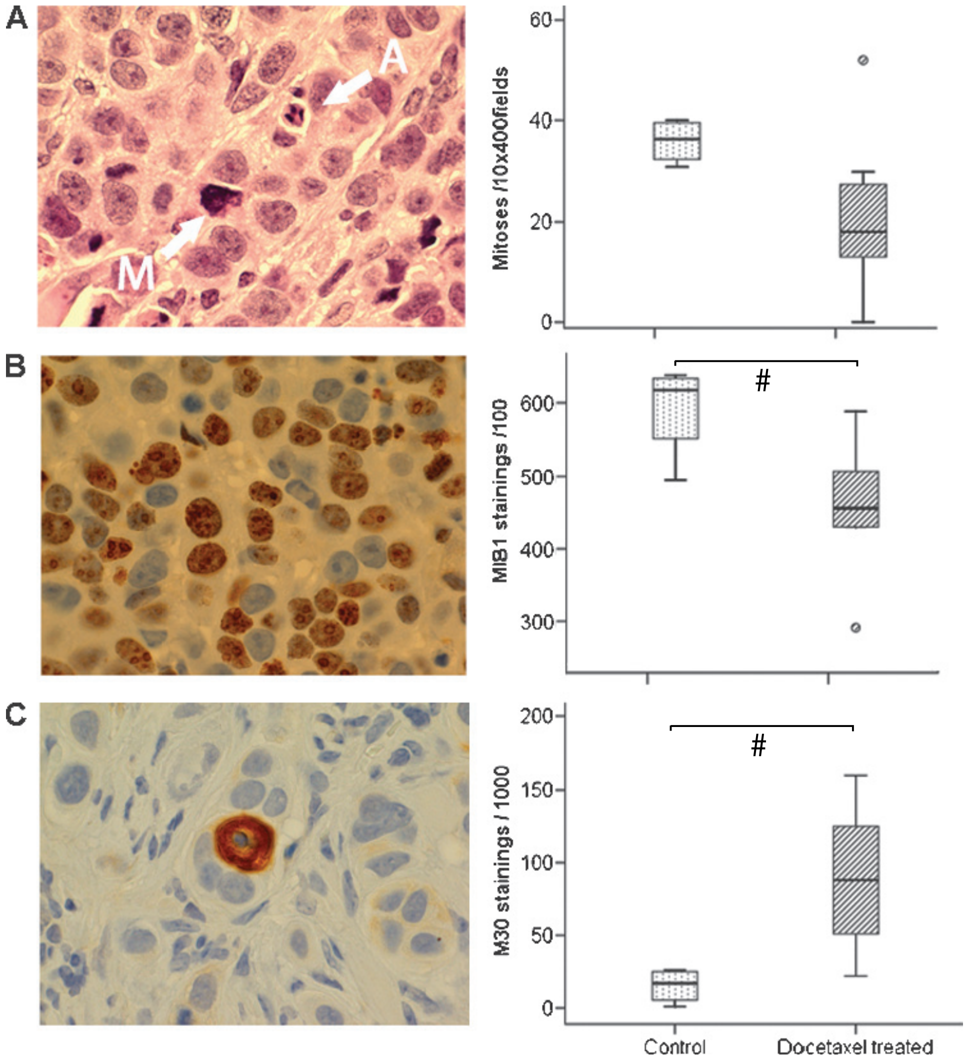

Figure 5. Histopathology 6 days after treatment of control ($n = 4$) and treated tumors ($n = 7$). (A) HES-stained section with apoptotic (A) and mitotic (M) cells. A trend of higher number of mitoses was detected in control tumors than in treated ($P = .065$) was detected. (B) Nuclear staining with Ki-67 MIB1 showing extensive proliferative activity. The control tumors had significantly higher proliferation than the treated ($P = .024$). (C) M30 cytodeath–stained section showing positive staining in the cytoplasm of an apoptotic cell. Control tumors had a significantly lower apoptotic index than the treated ($P < .01$). #Significant difference (t test) between the two groups. ○ indicates observations of 1.5 interquartile ranges from the end of the box.

Figure 2 summarizes the results from the DCE modeling. The progress during the week of follow-up indicated a trend of decreasing v_e in the control tumors, with the largest difference compared with the treated tumors 6 days after treatment ($P = .053$). No differences were found in K^{trans} before and after treatment or between the two groups for the semiquantitative parameters AUC, time to peak, and RSI. One tumor examined before treatment was excluded from the analysis because the volume (86 mm^3) was too small to obtain *in vivo* MRS or precise ROIs. Three DCE measurements were excluded because of unsuccessful contrast injection (a treated tumor 3 days after treatment, a control tumor, and a treated tumor 6 days after treatment).

Treated tumors had a significantly increased median ADC 3 and 6 days after treatment compared with before treatment ($P < .005$ and $P < .001$, respectively; Figure 3*A*). There were no changes in the control tumors during the follow-up. A significant difference was observed between the two groups 3 and 6 days after treatment ($P < .0005$ and $P < .05$, respectively). ADC maps of a control tumor and treated tumor before and 3 days after treatment are shown in Figure 3, *B* and *C*. The DW-MRI from a control tumor 1 day after treatment was excluded because of severe ghosting artifacts. In addition, the ADC values from a control tumor at days 3 and 6 after treatment were identified as outliers (extremely high ADC values, $P < .01$).

Treated tumors showed a drop in tCho levels measured by *in vivo* MRS 3 days after treatment and a slight increase from 3 to 6 days after treatment (Figure 4*A*). By comparing tCho levels in the two groups, the largest change was found during the day 1 to day 3 posttreatment period (mean decrease of 38%), but a significant difference in tCho was only observed between the treated and control tumors at day 6 after treatment ($P < .05$, t test). One tumor was excluded from the statistical analysis because of a very high initial level of tCho. However, this tumor followed the same trend as the others.

Ex Vivo HR MAS MRS

The HR MAS MR pulse-acquired spectra indicated a lower, although not significant, GPC, PCho, and Cho level in the treated tumors (Figure 4*C*). A higher –$(CH_2)_n$ and –CH_3 fatty acid content were also observed (Figure 4*D*).

Histopathologic Examinations

The histopathologic results are summarized in Figure 5. The proliferation index 6 days after treatment was significantly lower ($P < .05$) in the treated tumors (mean ± SD of 458 ± 95 MIB1-stained cells per 1000 cells) compared with controls (mean ± SD of 592 ± 66). In addition, treated tumors had a trend of lower number of mitotic cells (mean ± SD of 21.6 ± 16.7 per 10 × 400 fields) than the controls (mean ± SD of 36.0 ± 4.2, $P = .065$). Furthermore, the treated tumors had a significantly higher ($P < .01$) apoptotic index (mean ± SD of 88.9 ± 53.0 stained cells per 1000 cells) compared with controls (mean ± SD of 15.3 ± 11.9).

Correlation between MR Extracted Parameters and Histopathology

There were significant correlations between the median v_e and the number of mitoses ($r = -0.632$, $P < .05$) and the proliferation index ($r = -0.601$, $P < .05$) and the apoptotic index ($r = 0.674$, $P < .05$). K^{trans}, ADC, and tCho were not correlated with any of the histopathologic parameters.

A PLS model relating spectra and mitotic cells (five PCs) explained 94% and 100% of the *X* and *Y* variance, respectively. The *ex vivo* HR MAS MRS–predicted *versus* histologically measured number of mitotic cells was significantly correlated (calibration $r = 0.999$/validation $r = 0.935$, $P < .001$; Figure 6*A*). Tumors characterized by a high number of mitoses had a high score for PC1, and the corresponding loading profile showed higher concentrations of GPC, PCho, creatine, and taurine (Figure 6, *B* and *C*). A PLS model relating spectra and apoptotic index (4 PCs) explained 98% and 97% of the *X* and *Y* variance, respectively. The *ex vivo* HR MAS MRS–predicted *versus* histologically measured apoptotic index was significantly correlated (calibration $r = 0.946$/validation $r = 0.680$, $P < .05$; Figure 7*A*). Tumors characterized by a high apoptotic index had a high score for PC1, and the corresponding loading profile showed higher concentrations of –$(CH_2)_n$ and –CH_3 fatty acids (Figure 7, *B* and *C*). A PLS model relating spectra to the proliferation index (four PCs) explained 94% and 97% of the *X* and *Y* variance, respectively. There was a correlation between the *ex vivo* HR MAS MRS–predicted and the measured proliferation index (calibration $r = 0.978$/validation $r = 0.651$, $P = .058$; Figure 8*A*).

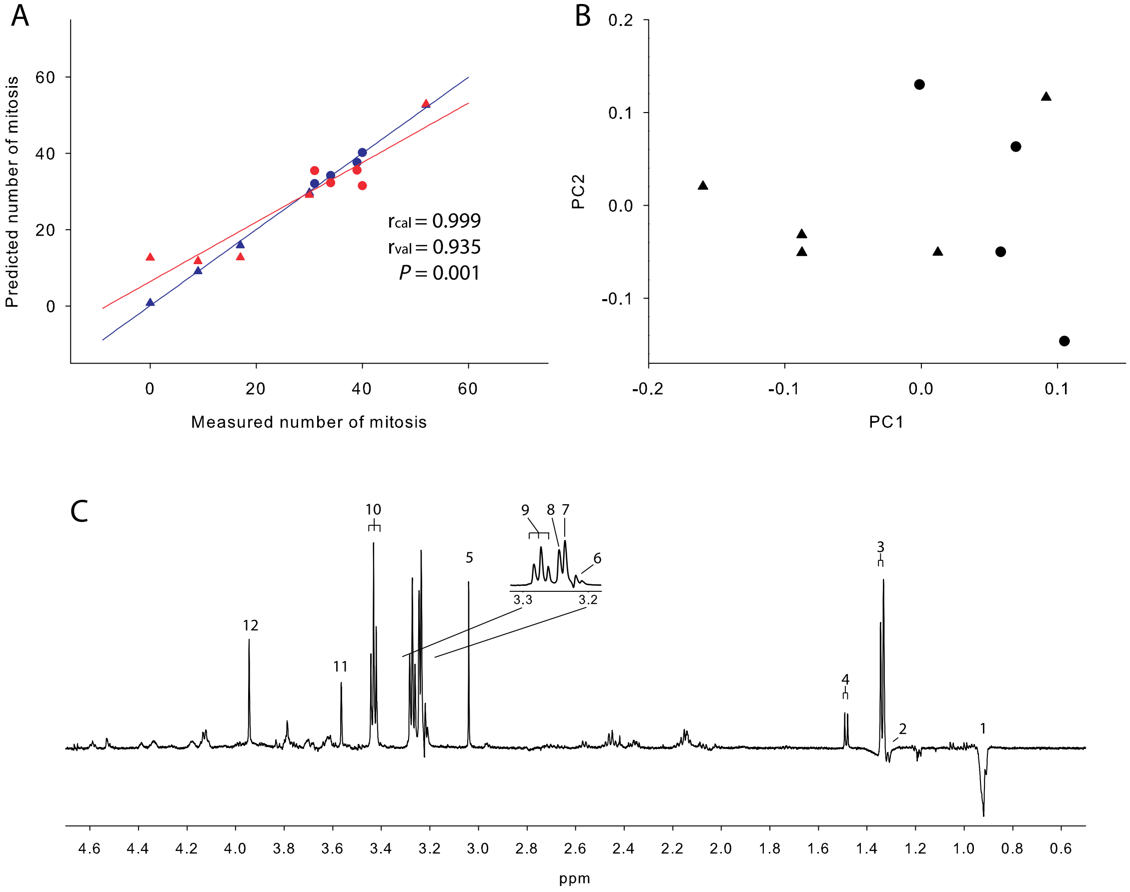

Figure 6. Results from the PLS regression analysis of HR MAS MR spin-echo spectra (spectral region 0.5-4.7 ppm) and the number of mitoses. (A) The predicted *versus* the measured number of mitoses for the calibration (red) and validation (blue). The Pearson correlation coefficients for the calibration (r_{cal}), validation (r_{val}), and the *P* value for the validation are marked. The total residual variance and root mean square error of prediction were minimized by retaining five PCs in the model. These five PCs accounted for 94% of the total *X* variation and 100% of the total *Y* variation. (B) Score plot of the PC1 *versus* PC2 from the PLS analysis. (C) The corresponding loading profile of PC1 illustrates that tumors with many mitoses have higher concentrations of GPC, PCho, creatine, and taurine. The following metabolites are assigned in the loading profile (peak number in parentheses): (1, 2) fatty acids, (3) lactate, (4) alanine, (5, 12) creatine, (6) choline, (7) PCho, (8) GPC, (9, 10) taurine, and (11) glycine. In panels A and B, ● control tumors and ▲ treated tumors.

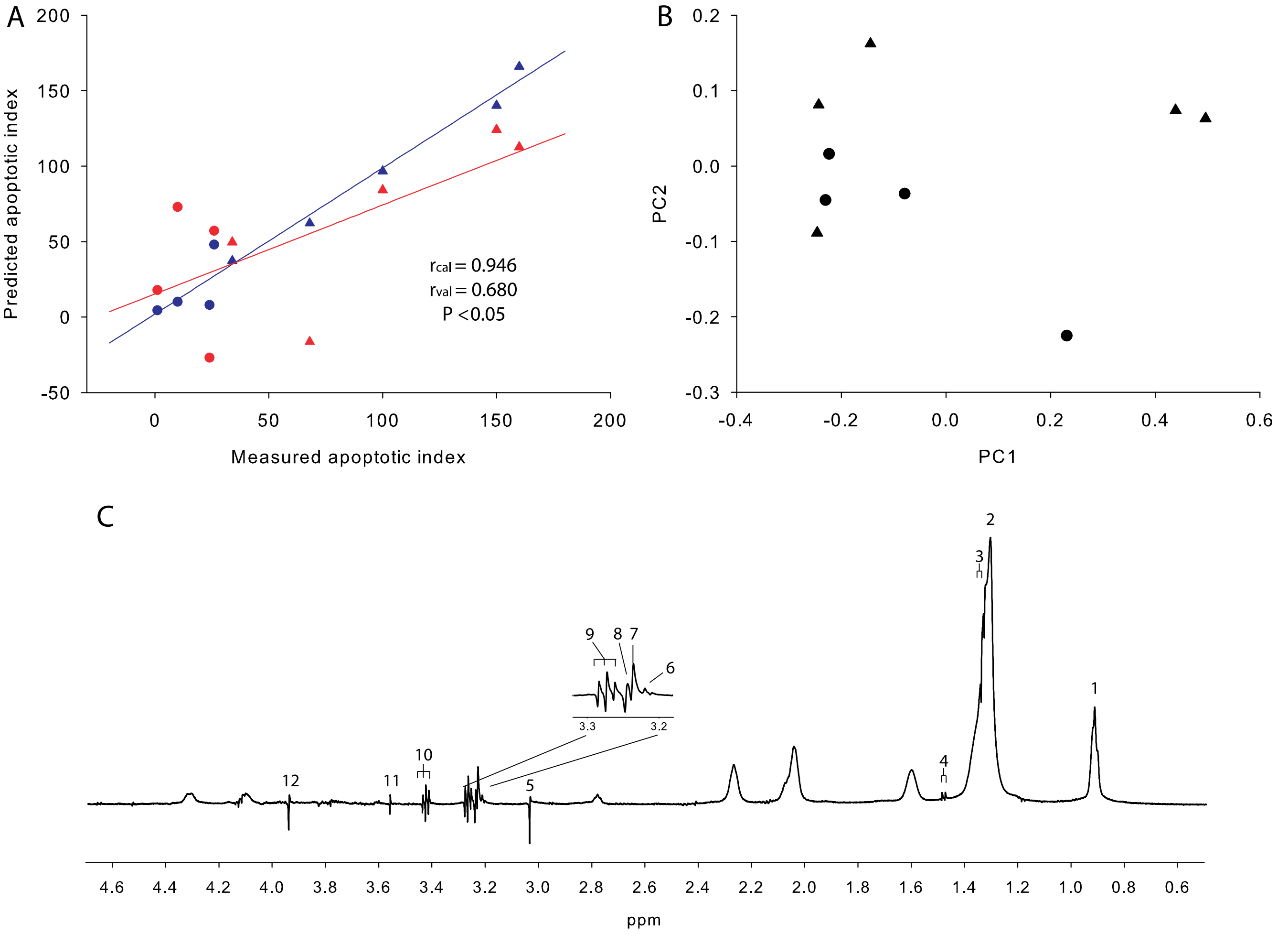

Figure 7. Results from the PLS regression analysis of HR MAS MR pulse-acquired spectra (spectral region 0.5-4.7 ppm) and the apoptotic index. (A) The predicted *versus* the measured apoptotic index for the calibration (red) and validation (blue). The Pearson correlation coefficients for the calibration (r_{cal}), validation (r_{val}), and the P value for the validation are marked. Total residual variance and root mean square error of prediction were minimized by retaining four PCs in the model. These four PCs accounted for 98% of the total X variation and 97% of the total Y variation. (B) Score plot of the PC1 *versus* PC2 from the PLS analysis. (C) The corresponding loading profile of PC1 illustrates that tumors with a high apoptotic index have higher concentrations of $-(CH_2)_n$ and $-CH_3$ fatty acids. The metabolites that are assigned with numbers are listed in the legend of Figure 6. In panels A and B, ● control tumors and ▲ treated tumors.

Tumors with a high proliferation index had a higher score for PC1 and were dominated by higher concentrations of GPC, PCho, and taurine (Figure 8, *B* and *C*). One tumor was defined as an outlier by the extreme studentized deviate procedure and was excluded.

Gene Expression Analysis

Among the 22,000 genes investigated, 107 were found to be significantly different between the control and treated tumors. Among these genes, 56 were downregulated and 51 were upregulated. Table 1 lists the genes of interest for docetaxel treatment based on literature describing processes such as angiogenesis, apoptosis, cell cycle, proliferation, microtubule reorganization, and tumor metabolism related to treatment response. The results of the GSEA did not provide any gene sets that were significantly enriched. Gene expression data were correlated to metabolite levels on the same samples using PLS. Cross-validation revealed no predictive ability (q^2 = 0.11), and testing of individual genes using moderated Hotelling T^2 statistic found no significant individual genes [37]. Two samples with an RNA integrity number lower than 6 were excluded from the analysis (treated tumors).

Discussion

The methods used in this study showed increased diffusion, altered metabolic and gene expression profiles, increased apoptosis, and decreased proliferation in a human breast cancer model treated with docetaxel, despite no significant change in tumor volume. The docetaxel treatment effects on the tumor microenvironment detected by DW-MRI were greatest 3 days after treatment and tended to fade out 6 days after treatment. No significant change in tumor volume indicates that a single i.p. dose of 30 mg/kg docetaxel initiates only minor treatment effects. Jensen et al. found significant differences in growth after docetaxel treatment. The tumors included in that study were larger than those used here, and thus, the lack of change in tumor volume differences here might be due to a higher relative measurement uncertainty. However, histopathology verified a docetaxel effect observed as a significantly lower proliferation index and higher apoptotic index after treatment.

A decreased v_e in controls corresponds to a decreased space available for the contrast agent, which is in accordance with the high proliferation seen in controls. The negative correlation between the v_e

and the number of mitoses and also the proliferation index, together with the positive correlation between the v_e and apoptosis, confirms that the v_e is related to changes in the tumor microenvironment. The lack of difference in K^{trans} between the two groups indicates the limited changes in the tumor vasculature. Other studies have shown that docetaxel has antiangiogenic effects [20,38] causing decreased K^{trans} in tumors [25,39]. However, changes in tumor vasculature caused by a single i.p. injection may be too small to be detected by current methodologies. Jensen et al. found a trend to increase in both v_e and K^{trans} after treatment, given a higher dose of docetaxel (40 mg/kg) [6]. Gadodiamide, a small molecule contrast agent, was chosen because it is widely used in the clinic. A contrast agent with a higher molecular weight would change the conditions for the model [22], improving the sensitivity for changes in K^{trans}.

The increased median ADC values of the treated tumors 3 and 6 days after treatment are consistent with the increased tissue water mobility, which can be caused by a loss of cell volume, breakdown of the plasma membrane, or cell death [15], confirmed by the decreased proliferation index and increased apoptotic index found by histopathology. However, there was no significant correlation between the ADC and any histopathologic parameter, indicating that the absolute value of the ADC is influenced by more than increased apoptosis and decreased proliferation. The increase in the ADC shortly after treatment is in accordance with previous findings [15,40] and supports DW-MRI as a suitable method for monitoring early docetaxel treatment effects.

The *in vivo* tCho signal depends on the cellular concentration of GPC, PCho, and Cho. GPC is a membrane breakdown product, whereas PCho is also a precursor of the membrane component phosphatidylcholine. Decreased tCho levels after docetaxel treatment is in accordance with earlier findings [6] and supports the hypothesis that MRS can observe changes in metabolism. The decreased tCho could also be due to less cell density, which is in agreement with histopathology and the increase in the v_e and ADC after treatment.

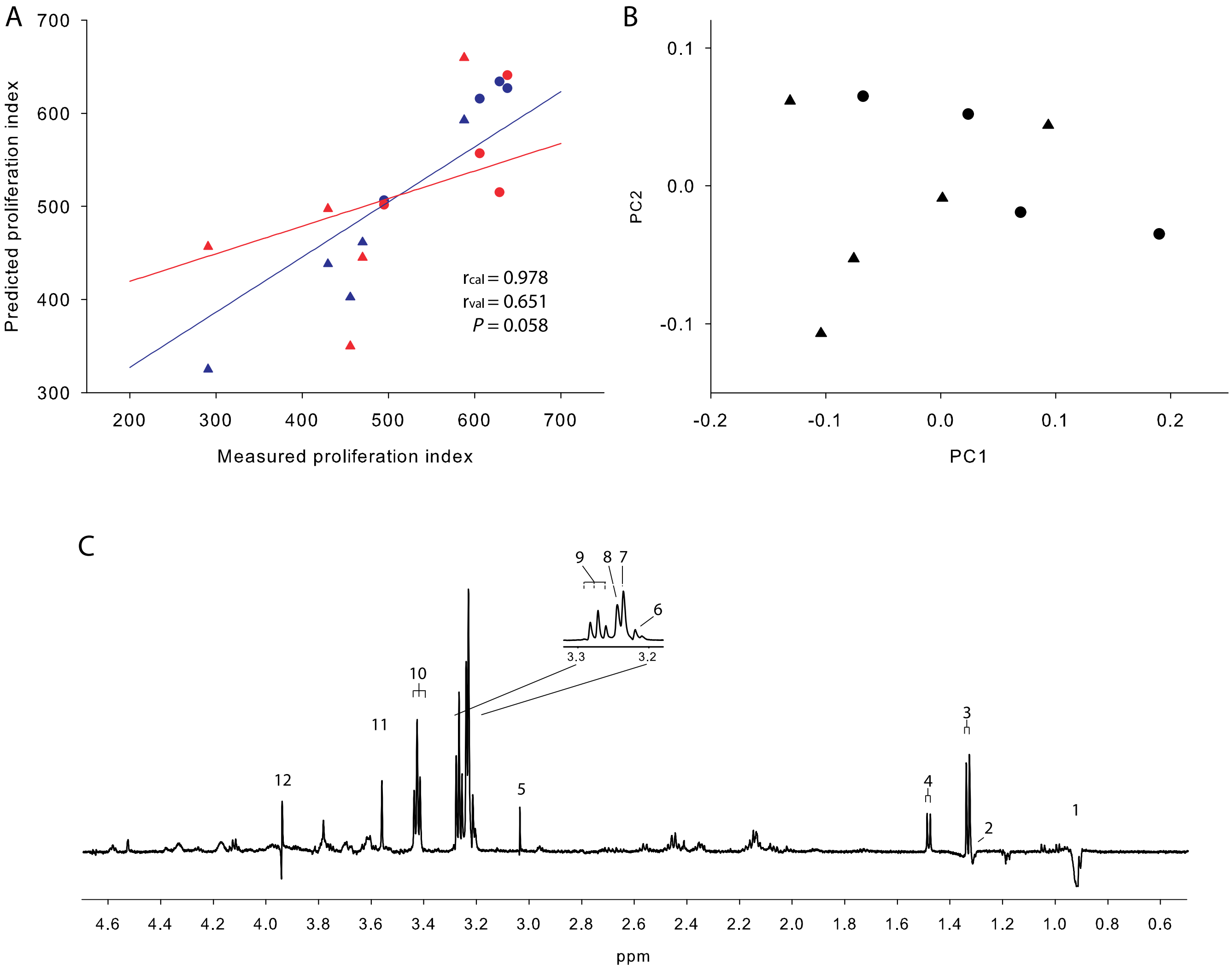

Figure 8. Results from the PLS regression analysis of HR MAS MR spin-echo spectra (spectral region 0.5-4.7 ppm) and the proliferation index. (A) The predicted *versus* measured the proliferation index for the calibration (red) and validation (blue). The Pearson correlation coefficients for the calibration (r_{cal}), validation (r_{val}), and the P value for the validation are marked. Total residual variance and root mean square error of prediction were minimized by retaining four PCs in the model. These four PCs accounted for 84% of the total X variation and 96% of the total Y variation. (B) Score plot of the PC1 *versus* PC2 from the PLS analysis. (C) The corresponding loading profile of PC1 illustrates that tumors with a high proliferation index have a higher concentration of GPC, PCho, and taurine. The metabolites that are assigned with numbers are listed in the legend of Figure 6. In panels A and B, ● control tumors and ▲ treated tumors.

Table 1. A Selection of Differentially Expressed Genes Related to Cancer and Docetaxel Treatment Response.

Gene	Full Name	Description	Up/Down	*P*	Gene ID and Additional References
TNFSF10	Tumor necrosis factor receptor superfamily member 10	Also known as TRIAL, protein inducing apoptosis in tumor cells.	Up	.04	8743 [50]
CASP6	Caspase 6 apoptosis-related cysteine peptidase	Involved in late apoptosis.	Up	.02	839 [51,52]
CARD8	Caspase recruitment domain family member 8	Encodes an adaptor molecule that suppresses apoptosis.	Down	.04	22900 [53]
GAS2L1	Growth arrest-specific 2 like 1	Encodes an actin-associated protein expressed at high levels in growth-arrested cells.	Down	.01	10634 [45,46,54,55]
CDC45L	Cell division cycle 45-like	Encodes a proliferation-associated protein (Cdc45) present in proliferating cells and plays a critical role in DNA replication by ensuring that chromosomal DNA is replicated only once per cell cycle.	Down	.02	8318 [56,57]
GOLGA3	Golgi autoantigen, golgin subfamily a3	Encodes the protein golgin-160, which is important for interactions between the Golgi and microtubules and thought to be important for reorganization of the Golgi during mitosis. Cleavage of golgin-160 also plays an important part in events leading to apoptosis.	Down	.04	2802 [58,59]
KIF4A	Kinesin family member 4A	Encodes a microtubule-based motor protein that generates directional movement along microtubules.	Down	.03	24137 [60]
GOLGB1	Golgin B1, golgi integral membrane protein	Encodes the protein giatin, which is involved in Golgi structure and trafficking.	Up	.04	2804 [61]
GBP2	Guanylate binding protein 2	GBP2 is the main transcriptional activator of the interferon encoded by *IFR1*. Interferons are cytokines that inhibit tumor cell proliferation.	Up	.00	2634 [61,62]
GHRL	Ghrelin/obestatin prepropeptide	Encodes the protein obestatin, which is involved many processes affecting cell proliferation.	Up	.03	51738 [63,64]
INTS6	Integrator complex subunit 6	A candidate tumor suppressor gene.	Down	.04	26512 [65,66]
TAOK2	TAO kinase 2	Has a role in cell signaling, microtubule organization and stability, and apoptosis.	Down	.03	9344
RPS6KA1	Ribosomal protein S6 kinase, 90 kDa, polypeptide 1	Implicated in controlling cell growth and differentiation.	Down	.04	6195
RPS6KA5	Ribosomal protein S6 kinase, 90 kDa, polypeptide 5	Involved in signal transduction and located in the MAPK signaling pathways. Related to cancer.	Up	.02	9252
EVI1	Ecotropic viral integration site 1	Increased copy number and transcript levels are associated with improved patient outcomes.	Up	.03	2122 [67]
SUFU	Suppressor of fused homolog	Associated with cancer-predisposing syndromes.	Down	.01	51684
PIAS4	Protein inhibitor of activated STAT, 4	Involved in signal transduction and related to cancer.	Down	.03	515888
DDR1	Discoidin domain receptor tyrosine kinase 1	Encodes a receptor tyrosine kinase (RTK) involved in regulation of cell growth, differentiation, and metabolism. RTKs are important for communication between cells and their microenvironment.	Down	.05	780
LIPF	Lipase, gastric	Encodes gastric lipase, which hydrolyzes the ester bonds of triglycerides under acidic pH conditions.	Up	.02	8513 [42]
ACLY	ATP citrate lyase	Involved in metabolism.	Down	.02	47
BTN2A2	Butyrophilin, subfamily 2, member A2	Encodes a type 1 receptor glycoprotein involved in lipid, fatty acid and sterol metabolism.	Up	.01	10385

The decrease in PCho and Cho after treatment is in accordance with earlier findings [9,41]; however, these studies reported increased GPC after treatment. Consistent with our findings, Jensen et al. [6] reported decreased GPC in docetaxel-treated MCF7 xenografts. The absence of significant changes in GPC, PCho, and Cho levels in the *ex vivo* tissues could be due to late biopsy harvest (6 days after treatment) or due to tumor heterogeneity. The PLS score values and corresponding loading profiles substantiate that highly proliferative tumors with many mitoses have a higher concentration of GPC, PCho, and Cho. It has been previously observed that PCho and Cho levels increase with tumor malignancy [7,36] because of the stimulation of choline transport caused by the up-regulation of choline transporters encoded by *SLC5A7* and *SLC22A2* and choline phosphorylation caused by the enzyme choline kinase alpha [36] encoded by *CHKA*. No such differences in gene expression between the two groups were found to explain the differences in choline metabolism in our study. Our results are in accordance with an *in vitro* study of docetaxel-treated MCF7 cells using polymerase chain reaction [12]. Taken together, these findings suggest that the decreased level of GPC, PCho, and Cho after docetaxel treatment might be caused by a mechanism other than the regulation of genes involved in the glycerophospholipid metabolic pathway.

Consistent with the histopathology, the expression levels of genes involved in the cell cycle and proliferation indicate decreased proliferation in treated tumors. Interactions between the Golgi and microtubules are important for the postfragmentation reorganization of the Golgi during mitosis. The expression of *GOLGA3*, *GOLGB1*, and *KIF4A* indicates decreased movement along the microtubules, which also agrees with the expected docetaxel treatment effects [5].

Tumors with high apoptotic activity had a higher content of $–(CH_2)_n$ and $–CH_3$ fatty acids. Mean *ex vivo* HR MAS MR spectra and PLS analysis relating apoptotic index to the spectra showed a clear difference in lipid content. Lipase gastric (*LIPF*), which is involved in glycerolipid metabolism [42] and hydrolyzes the ester bonds of triglycerides into fatty acids, was found to be significantly upregulated in treated cells. This finding might explain the elevated levels of $–(CH_2)_n$ and $–CH_3$ fatty acids in the docetaxel-treated tumors and may be related to the elevated apoptotic index. Previous studies in glioma models have shown increased lipid content to be a function of a high apoptotic cell fraction [43]. Also, HR MAS MRS of human cervical cancer specimens has revealed similar correlations [44].

Four genes known to be involved in apoptosis were found to be differentially expressed between the two groups, and their up- and down-regulation indicate increased apoptotic activity after treatment (Table 1), which is in agreement with the histopathology. *TNFSF10* and *CASP6*, together with tumor necrosis factor receptor superfamily member 10b (*TNFRSF10B*, $P = .088$), were located along the caspase-mediated apoptotic pathway. Thus, three of six genes along the same apoptotic pathway were upregulated. In addition, *GAS2L* was found to be significantly downregulated. This gene encodes growth arrest–specific protein 2 (Gas2), which colocalizes with actin at the cell border and along stress fibers in growth-arrested cells. *GAS2L1* is highly upregulated in growth-arrested cells *in vitro*; however, it becomes downregulated when arrested cells reenter the cell cycle [45,46]. This indicates that the mitotic arrest caused by docetaxel is about to be almost eliminated 6 days after treatment, which is in accordance with the upregulation of late apoptosis-related *CASP6*. This may also explain why other genes related to growth arrest, for instance major protein kinase C substrate (*MARCKS*) [47], were not significantly changed.

Increased apoptosis 6 days after treatment was confirmed with HR MAS MRS, gene expression, and immunohistochemistry. However, a study of MCF7 xenografts by Morse et al. [48] found no apoptotic activity after docetaxel treatment. They analyzed biopsies grown in the mammary fat pad, 2 days after treatment, in contrast to the subcutaneous model used in the present study. In addition, the MCF7 cell lines used in the two studies were obtained from different laboratories; thus, the tumors may have different biologic properties [49]. Furthermore, *in vitro* cell studies from Hernandez-Vargas et al. [13] showed dose dependency in the mechanism of cell death after docetaxel treatment. Low doses (4 nM) induced mitotic catastrophe followed by necrosis, and high doses (100 nM) induced apoptosis.

Docetaxel has been found to have antiangiogenic effects [20,38]. In our study, no genes in the vascular endothelial growth factor pathway as listed in the Kyoto Encyclopedia of Genes and Genomes [33–35] were found to be significantly different between the two groups. These data are in agreement with K^{trans} values, which exhibited no change. Thus, our study suggests limited antiangiogenic effects in tumors after a single docetaxel treatment.

Conclusions

This study shows that *in vivo* MRS, DW-MRI, and *ex vivo* HR MAS MRS are suitable for monitoring early docetaxel treatment effects, which is promising for translation into the clinic. The histopathologic results show that an i.p. dose of 30 mg/kg of docetaxel induced apoptosis and decreased proliferation in MCF7 xenografts. Of the three time points chosen for MRI/MRS examination, 3 days after treatment seems to be most suitable for detecting docetaxel treatment effects and the effects fade 6 days after treatment. The gene expression analysis yields a better understanding of the results found by the multimodal imaging methods.

Acknowledgments

The authors thank Unn Granli and Borgny Ytterhus at the Department of Laboratory Medicine, Children's and Women's Health, Norwegian University of Science and Technology, for staining of the histology sections.

References

[1] Parkin DM, Bray F, Ferlay J, and Pisani P (2005). Global cancer statistics, 2002. *CA Cancer J Clin* **55**(2), 74–108.

[2] Crown J and O'Leary M (2000). The taxanes: an update. *Lancet* **355**(9210), 1176–1178.

[3] Moulder S and Hortobagyi GN (2008). Advances in the treatment of breast cancer. *Clin Pharmacol Ther* **83**(1), 26–36.

[4] Estevez LG and Gradishar WJ (2004). Evidence-based use of neoadjuvant taxane in operable and inoperable breast cancer. *Clin Cancer Res* **10**(10), 3249–3261.

[5] Hernandez-Vargas H, Palacios J, and Moreno-Bueno G (2007). Telling cells how to die: docetaxel therapy in cancer cell lines. *Cell Cycle* **6**(7), 780–783.

[6] Jensen LR, Huuse EM, Bathen TF, Goa PE, Bofin AM, Pedersen TB, Lundgren S, and Gribbestad IS (2010). Assessment of early docetaxel response in an experimental model of human breast cancer using DCE-MRI, *ex vivo* HR MAS, and *in vivo* 1H MRS. *NMR Biomed* **23**(1), 56–65.

[7] Glunde K and Serkova NJ (2006). Therapeutic targets and biomarkers identified in cancer choline phospholipid metabolism. *Pharmacogenomics* **7**(7), 1109–1123.

[8] Negendank W (1992). Studies of human tumors by MRS: a review. *NMR Biomed* **5**(5), 303–324.

[9] Morse DL, Raghunand N, Sadarangani P, Murthi S, Job C, Day S, Howison C, and Gillies RJ (2007). Response of choline metabolites to docetaxel therapy is quantified *in vivo* by localized (31)P MRS of human breast cancer xenografts and *in vitro* by high-resolution (31)P NMR spectroscopy of cell extracts. *Magn Reson Med* **58**(2), 270–280.

[10] Glunde K, Jie C, and Bhujwalla ZM (2004). Molecular causes of the aberrant choline phospholipid metabolism in breast cancer. *Cancer Res* **64**(12), 4270–4276.

[11] Glunde K, Ackerstaff E, Mori N, Jacobs MA, and Bhujwalla ZM (2006). Choline phospholipid metabolism in cancer: consequences for molecular pharmaceutical interventions. *Mol Pharm* **3**(5), 496–506.

[12] Morse DL, Carroll D, Day S, Gray H, Sadarangani P, Murthi S, Job C, Baggett B, Raghunand N, and Gillies RJ (2009). Characterization of breast cancers and therapy response by MRS and quantitative gene expression profiling in the choline pathway. *NMR Biomed* **22**(1), 114–127.

[13] Hernandez-Vargas H, Palacios J, and Moreno-Bueno G (2007). Molecular profiling of docetaxel cytotoxicity in breast cancer cells: uncoupling of aberrant mitosis and apoptosis. *Oncogene* **26**(20), 2902–2913.

[14] Morse DL, Gray H, Payne CM, and Gillies RJ (2005). Docetaxel induces cell death through mitotic catastrophe in human breast cancer cells. *Mol Cancer Ther* **4**(10), 1495–1504.

[15] Galons JP, Altbach MI, Paine-Murrieta GD, Taylor CW, and Gillies RJ (1999). Early increases in breast tumor xenograft water mobility in response to paclitaxel therapy detected by non-invasive diffusion magnetic resonance imaging. *Neoplasia* **1**(2), 113–117.

[16] Kim H, Morgan DE, Zeng H, Grizzle WE, Warram JM, Stockard CR, Wang D, and Zinn KR (2008). Breast tumor xenografts: diffusion-weighted MR imaging to assess early therapy with novel apoptosis-inducing anti-DR5 antibody. *Radiology* **248**(3), 844–851.

[17] Pickles MD, Gibbs P, Lowry M, and Turnbull LW (2006). Diffusion changes precede size reduction in neoadjuvant treatment of breast cancer. *Magn Reson Imaging* **24**(7), 843–847.

[18] Yankeelov TE, Lepage M, Chakravarthy A, Broome EE, Niermann KJ, Kelley MC, Meszoely I, Mayer IA, Herman CR, McManus K, et al. (2007). Integration of quantitative DCE-MRI and ADC mapping to monitor treatment response in human breast cancer: initial results. *Magn Reson Imaging* **25**(1), 1–13.

[19] Padhani AR, Liu G, Koh DM, Chenevert TL, Thoeny HC, Takahara T, Dzik-Jurasz A, Ross BD, Van CM, Collins D, et al. (2009). Diffusion-weighted magnetic resonance imaging as a cancer biomarker: consensus and recommendations. *Neoplasia* **11**(2), 102–125.

[20] Hotchkiss KA, Ashton AW, Mahmood R, Russell RG, Sparano JA, and Schwartz EL (2002). Inhibition of endothelial cell function *in vitro* and angiogenesis *in vivo* by docetaxel (Taxotere): association with impaired repositioning of the microtubule organizing center. *Mol Cancer Ther* **1**(13), 1191–1200.

[21] Turnbull LW (2009). Dynamic contrast-enhanced MRI in the diagnosis and management of breast cancer. *NMR Biomed* **22**(1), 28–39.

[22] Tofts PS (1997). Modeling tracer kinetics in dynamic Gd-DTPA MR imaging. *J Magn Reson Imaging* **7**(1), 91–101.

[23] Hayes C, Padhani AR, and Leach MO (2002). Assessing changes in tumour vascular function using dynamic contrast-enhanced magnetic resonance imaging. *NMR Biomed* **15**(2), 154–163.

[24] Martincich L, Montemurro F, De RG, Marra V, Ponzone R, Cirillo S, Gatti M, Biglia N, Sarotto I, Sismondi P, et al. (2004). Monitoring response to primary chemotherapy in breast cancer using dynamic contrast-enhanced magnetic resonance imaging. *Breast Cancer Res Treat* **83**(1), 67–76.

[25] Pickles MD, Lowry M, Manton DJ, Gibbs P, and Turnbull LW (2005). Role of dynamic contrast enhanced MRI in monitoring early response of locally advanced breast cancer to neoadjuvant chemotherapy. *Breast Cancer Res Treat* **91**(1), 1–10.

[26] Kuhl CK, Mielcareck P, Klaschik S, Leutner C, Wardelmann E, Gieseke J, and Schild HH (1999). Dynamic breast MR imaging: are signal intensity time course data useful for differential diagnosis of enhancing lesions? *Radiology* **211**(1), 101–110.

[27] Jensen LR, Berge K, Bathen TF, Wergedahl H, Schonberg SA, Bofin A, Berge RK, and Gribbestad IS (2007). Effect of dietary tetradecylthioacetic acid on colon cancer growth studied by dynamic contrast enhanced MRI. *Cancer Biol Ther* **6**(11), 1810–1816.

[28] Mayr NA, Yuh WT, Arnholt JC, Ehrhardt JC, Sorosky JI, Magnotta VA, Berbaum KS, Zhen W, Paulino AC, Oberley LW, et al. (2000). Pixel analysis of MR perfusion imaging in predicting radiation therapy outcome in cervical cancer. *J Magn Reson Imaging* **12**(6), 1027–1033.

[29] Sitter B, Lundgren S, Bathen TF, Halgunset J, Fjosne HE, and Gribbestad IS (2006). Comparison of HR MAS MR spectroscopic profiles of breast cancer tissue with clinical parameters. *NMR Biomed* **19**(1), 30–40.

[30] Smyth GK (2004). Linear models and empirical Bayes methods for assessing differential expression in microarray experiments. *Stat Appl Genet Mol Biol* **3**, Article 3.

[31] Benjamini Y and Hochberg Y (1995). Controlling the false discovery rate: a practical and powerful approach to multiple testing. *J R Stat Soc Series B Stat Methodol* **57**, 289–300.

[32] Subramanian A, Tamayo P, Mootha VK, Mukherjee S, Ebert BL, Gillette MA, Paulovich A, Pomeroy SL, Golub TR, Lander ES, et al. (2005). Gene set enrichment analysis: a knowledge-based approach for interpreting genome-wide expression profiles. *Proc Natl Acad Sci USA* **102**(43), 15545–15550.

[33] Kanehisa M and Goto S (2000). KEGG: Kyoto Encyclopedia of Genes and Genomes. *Nucleic Acids Res* **28**(1), 27–30.

[34] Kanehisa M, Goto S, Hattori M, oki-Kinoshita KF, Itoh M, Kawashima S, Katayama T, Araki M, and Hirakawa M (2006). From genomics to chemical genomics: new developments in KEGG. *Nucleic Acids Res* **34**(database issue), D354–D357.

[35] Kanehisa M, Araki M, Goto S, Hattori M, Hirakawa M, Itoh M, Katayama T, Kawashima S, Okuda S, Tokimatsu T, et al. (2008). KEGG for linking genomes to life and the environment. *Nucleic Acids Res* **36**(database issue), D480–D484.

[36] Eliyahu G, Kreizman T, and Degani H (2007). Phosphocholine as a biomarker of breast cancer: molecular and biochemical studies. *Int J Cancer* **120**(8), 1721–1730.

[37] Gidskehaug L, Anderssen E, Flatberg A, and Alsberg BK (2007). A framework for significance analysis of gene expression data using dimension reduction methods. *BMC Bioinformatics* **8**, 346–359.

[38] Pasquier E, Honore S, and Braguer D (2006). Microtubule-targeting agents in angiogenesis: where do we stand? *Drug Resist Updat* **9**(1–2), 74–86.

[39] Maxwell RJ, Wilson J, Prise VE, Vojnovic B, Rustin GJ, Lodge MA, and Tozer GM (2002). Evaluation of the anti-vascular effects of combretastatin in rodent tumours by dynamic contrast enhanced MRI. *NMR Biomed* **15**(2), 89–98.

[40] Kim JK, Park SH, Lee HM, Lee YH, Sung NK, Chung DS, and Kim OD (2003). *In vivo* ^{1}H-MRS evaluation of malignant and benign breast diseases. *Breast* **12**(3), 179–182.

[41] Sterin M, Cohen JS, Mardor Y, Berman E, and Ringel I (2001). Levels of phospholipid metabolites in breast cancer cells treated with antimitotic drugs: a ^{31}P-magnetic resonance spectroscopy study. *Cancer Res* **61**(20), 7536–7543.

[42] Pafumi Y, Lairon D, de la Porte PL, Juhel C, Storch J, Hamosh M, and Armand M (2002). Mechanisms of inhibition of triacylglycerol hydrolysis by human gastric lipase. *J Biol Chem* **277**(31), 28070–28079.

[43] Hakumaki JM, Poptani H, Sandmair AM, Yla-Herttuala S, and Kauppinen RA (1999). ^{1}H MRS detects polyunsaturated fatty acid accumulation during gene therapy of glioma: implications for the *in vivo* detection of apoptosis. *Nat Med* **5**(11), 1323–1327.

[44] Lyng H, Sitter B, Bathen TF, Jensen LR, Sundfor K, Kristensen GB, and Gribbestad IS (2007). Metabolic mapping by use of high-resolution magic angle spinning ^{1}H MR spectroscopy for assessment of apoptosis in cervical carcinomas. *BMC Cancer* **7**, 11–22.

[45] Brancolini C, Bottega S, and Schneider C (1992). Gas2, a growth arrest–specific protein, is a component of the microfilament network system. *J Cell Biol* **117**(6), 1251–1261.

[46] Goriounov D, Leung CL, and Liem RK (2003). Protein products of human Gas2-related genes on chromosomes 17 and 22 (hGAR17 and hGAR22) associate with both microfilaments and microtubules. *J Cell Sci* **116**(pt 6), 1045–1058.

[47] Herget T, Brooks SF, Broad S, and Rozengurt E (1993). Expression of the major protein kinase C substrate, the acidic 80-kilodalton myristoylated alanine-rich C kinase substrate, increases sharply when Swiss 3T3 cells move out of cycle and enter G_0. *Proc Natl Acad Sci USA* **90**(7), 2945–2949.

[48] Morse DL, Galons JP, Payne CM, Jennings DL, Day S, Xia G, and Gillies RJ (2007). MRI-measured water mobility increases in response to chemotherapy via multiple cell-death mechanisms. *NMR Biomed* **20**(6), 602–614.

[49] Osborne CK, Hobbs K, and Trent JM (1987). Biological differences among MCF-7 human breast cancer cell lines from different laboratories. *Breast Cancer Res Treat* **9**(2), 111–121.

[50] Sheridan JP, Marsters SA, Pitti RM, Gurney A, Skubatch M, Baldwin D, Ramakrishnan L, Gray CL, Baker K, Wood WI, et al. (1997). Control of TRAIL-induced apoptosis by a family of signaling and decoy receptors. *Science* **277**(5327), 818–821.

[51] Cao XH, Wang AH, Wang CL, Mao DZ, Lu MF, Cui YQ, and Jiao RZ (2010). Surfactin induces apoptosis in human breast cancer MCF-7 cells through a ROS/JNK–mediated mitochondrial/caspase pathway. *Chem Biol Interact* **183**(3), 357–362.

[52] Lee SC, Chan J, Clement MV, and Pervaiz S (2006). Functional proteomics of resveratrol-induced colon cancer cell apoptosis: caspase-6–mediated cleavage of lamin A is a major signaling loop. *Proteomics* **6**(8), 2386–2394.

[53] Razmara M, Srinivasula SM, Wang L, Poyet JL, Geddes BJ, DiStefano PS, Bertin J, and Alnemri ES (2002). CARD-8 protein, a new CARD family member that regulates caspase-1 activation and apoptosis. *J Biol Chem* **277**(16), 13952–13958.

[54] Brancolini C, Benedetti M, and Schneider C (1995). Microfilament reorganization during apoptosis: the role of Gas2, a possible substrate for ICE-like proteases. *EMBO J* **14**(21), 5179–5190.

[55] Sgorbissa A, Benetti R, Marzinotto S, Schneider C, and Brancolini C (1999). Caspase-3 and caspase-7 but not caspase-6 cleave Gas2 *in vitro*: implications for microfilament reorganization during apoptosis. *J Cell Sci* **112**(pt 23), 4475–4482.

[56] Pollok S and Grosse F (2007). Cdc45 degradation during differentiation and apoptosis. *Biochem Biophys Res Commun* **362**(4), 910–915.

[57] Pollok S, Bauerschmidt C, Sanger J, Nasheuer HP, and Grosse F (2007). Human Cdc45 is a proliferation-associated antigen. *FEBS J* **274**(14), 3669–3684.

[58] Gillingham AK, Pfeifer AC, and Munro S (2002). CASP, the alternatively spliced product of the gene encoding the CCAAT-displacement protein transcription factor, is a Golgi membrane protein related to giantin. *Mol Biol Cell* **13**(11), 3761–3774.

[59] Maag RS, Mancini M, Rosen A, and Machamer CE (2005). Caspase-resistant Golgin-160 disrupts apoptosis induced by secretory pathway stress and ligation of death receptors. *Mol Biol Cell* **16**(6), 3019–3027.

[60] Lee YM, Lee S, Lee E, Shin H, Hahn H, Choi W, and Kim W (2001). Human kinesin superfamily member 4 is dominantly localized in the nuclear matrix and is associated with chromosomes during mitosis. *Biochem J* **360**(pt 3), 549–556.

[61] Rosing M, Ossendorf E, Rak A, and Barnekow A (2007). Giantin interacts with both the small GTPase Rab6 and Rab1. *Exp Cell Res* **313**(11), 2318–2325.

[62] Guimaraes DP, Oliveira IM, de ME, Paiva GR, Souza DM, Barnas C, Olmedo DB, Pinto CE, Faria PA, De Moura Gallo CV, et al. (2009). Interferon-inducible guanylate binding protein (GBP)-2: a novel p53-regulated tumor marker in esophageal squamous cell carcinomas. *Int J Cancer* **124**(2), 272–279.

[63] Malik NM, Moore GB, Kaur R, Liu YL, Wood SL, Morrow RW, Sanger GJ, and Andrews PL (2008). Adaptive upregulation of gastric and hypothalamic ghrelin receptors and increased plasma ghrelin in a model of cancer chemotherapy–induced dyspepsia. *Regul Pept* **148**(1–3), 33–38.

[64] Wagner K, Hemminki K, Grzybowska E, Klaes R, Burwinkel B, Bugert P, Schmutzler RK, Wappenschmidt B, Butkiewicz D, Pamula J, et al. (2006). Polymorphisms in genes involved in GH1 release and their association with breast cancer risk. *Carcinogenesis* **27**(9), 1867–1875.

[65] Wieland I, Sell C, Weidle UH, and Wieacker P (2004). Ectopic expression of DICE1 suppresses tumor cell growth. *Oncol Rep* **12**(2), 207–211.

[66] Wieland I, Ropke A, Stumm M, Sell C, Weidle UH, and Wieacker PF (2001). Molecular characterization of the *DICE1* (DDX26) tumor suppressor gene in lung carcinoma cells. *Oncol Res* **12**(11–12), 491–500.

[67] Nanjundan M, Nakayama Y, Cheng KW, Lahad J, Liu J, Lu K, Kuo WL, Smith-McCune K, Fishman D, Gray JW, et al. (2007). Amplification of MDS1/EVI1 and EVI1, located in the 3q26.2 amplicon, is associated with favorable patient prognosis in ovarian cancer. *Cancer Res* **67**(7), 3074–3084.